"Online, *In-Situ* Monitoring Combustion Turbines Using Wireless Passive Ceramic Sensors"

Final Report
Project Period: 1/1/2010-6/30/2013

Xun Gong (PI, Department of Electrical Engineering and Computer Science)
And
Linan An (Co-PI, Department of Materials Science and Engineering)
And
Chengying Xu (Co-PI, Department of Mechanical and Aerospace Engineering)

in November 2013

Program DE-FOA-0000059
Grant DE-FE0001241

Harris Corporation Engineering Center Room 426
Department of Electrical Engineering and Computer Science (EECS)
University of Central Florida (UCF)
4000 Central Florida Blvd.
Orlando, FL 32816-2362

Phone: (407) 823 5762
Fax: (407) 823 5835
Email: xun.gong@ucf.edu

Disclaimer

Abstract

The overall objective of this project is to develop high-temperature wireless passive ceramic sensors for online, real-time monitoring combustion turbines. During this project period, we have successfully demonstrated temperature sensors up to 1300^{o}C and pressure sensors up to 800^{o}C. The temperature sensor is based on a high-Q-factor dielectric resonator and the pressure sensor utilizes the evanescent-mode cavity to realize a pressure-sensitive high-Q-factor resonator. Both sensors are efficiently integrated with a compact antenna. These sensors are wirelessly interrogated. The resonant frequency change corresponding to either temperature or pressure can be identified using a time-domain gating technique. The sensors realized in this project can survive harsh environments characterized by high temperatures (>1000^{o}C) and corrosive gases, owing to the excellent material properties of polymer-derived ceramics (PDCs) developed at University of Central Florida. It is anticipated that this work will significantly advance the capability of high-temperature sensor technologies and be of a great benefit to turbine industry and their customers.

TABLE OF CONTENTS:

1. Executive Summary

This research project aims to develop *accurate* and *robust* wireless passive high-temperature (> 1300°C) microsensors for *in situ* measurement of temperature and pressure inside combustion turbines for power generation systems. Specifically, two types of wireless passive high-temperature sensors have been investigated based on recently-developed multifunctional polymer-derived ceramics (PDCs): one is a temperature sensor, and the other is a pressure sensor. It is expected that this research would lay down a solid foundation for the development of commercially-viable advanced sensor technologies for *in-situ* real-time monitoring of the operation of power generation systems thus providing precise operational parameters in real-time for optimal system control for higher efficiency, increased reliability, and reduced NO_x emission.

Research on PDCs has revealed that PDCs possess outstanding multifunctionality including ***excellent thermo-electrical properties*** at high temperatures (up to 1500°C) thus providing direct transduction mechanisms for design and fabrication of high-temperature sensors. In addition, they offer unique advantages such as ***ease of microfabrication*** and ***excellent corrosion resistance***. These properties make PDCs particularly suitable for microsensors that can be used at high temperatures. In this project period, the dielectric properties of the PDC materials were characterized at both high temperatures (up to 1150°C) and microwave frequencies (same as the operation frequencies of the temperature and pressure sensors). It was shown that the dielectric constant of the PDCs monotonically increases versus temperature, which was utilized to develop the wireless passive temperature sensor. Furthermore, we have studied the loss tangent of PDCs with different compositions and fabrication conditions. PDCs with lower loss tangents at high temperatures were selected to improve the Q factor of the temperature and pressure sensors.

In order to sense the temperature and pressure ***wirelessly*** with ***high accuracy***, high-Q microwave resonators sensitive to either temperature or pressure are necessary. In this project, dielectric resonator structure was used to realize high-Q temperature sensors. The resonant frequency of the dielectric resonator is primarily dependent on the size of the resonator and the dielectric constant of the PDC material. The aforementioned monotonic relationship between the temperature and dielectric constant provides a temperature sensing mechanism. A compact slot antenna was integrated on top of the temperature sensor to achieve high coupling efficiency between the sensor and antenna. The temperature sensors are able to measure temperatures up to 1300°C using a wireless interrogation method. The pressure sensors are based on the evanescent-mode cavity, in which the cavity deforms corresponding to external pressure. This deformation changes the gap dimension between the top of the cavity and post inside the cavity, therefore leading to a resonant frequency change. By wirelessly sensing the resonant frequency, we can find the pressure by characterizing the relationship between and pressure and resonant frequency. A compact patch/slot coupling structure was used to achieve the highest efficiency for this integrated antenna. The pressure sensors were fabricated in two pieces using micro mechanical machining before sintering. Then the machined pieces were sintered in furnace to realize robust PDCs. These pieces were then metallized using platinum paste. Finally, the two pieces were bonded to form the pressure sensor. These pressure sensors were characterized up to 800°C with different applied pressures. To facilitate the sensor measurement, a robust wide-band antenna was developed to cover the operation frequency range of temperature/pressure sensors up to 1300°C.

Development of sensors and sensor system for high-temperature and harsh environments has attracted extensive research activities in the past few years but with limited success. The current technologies for temperature and pressure measurement in power generation systems are limited to a low temperature range (< 800°C). The sensors developed in this project will advance the sensor technologies beyond the

current state in the following aspects: (i) significantly advance sensor technology for applications in harsh and high-temperature (> 1300^{o}C) environments; (ii) promote the use of newly-developed polymer-derived ceramics for highly sensitive, long term, *in-situ* and real-time monitoring of advanced power generation systems; (iii) achieve an in-depth understanding of material properties and microfabrication technology, as well as device development based on polymer-derived ceramics; (iv) effectively combine microwave technology with material development to achieve novel sensor capabilities; and (v) substantially benefit the turbine industries and their customers by ultimately providing sensing technology for potential performance improvement.

2. Report Details

2.1. High Temperature PDC Characterization

Fig. 1 shows the metallized SiCN resonator and CPW lines used for calibration and measurement. In this project, we characterized the PDC material properties up to 1400°C (observed responses up to 1300°C). The dimensions of the SiCN resonator are presented in Fig. 2.

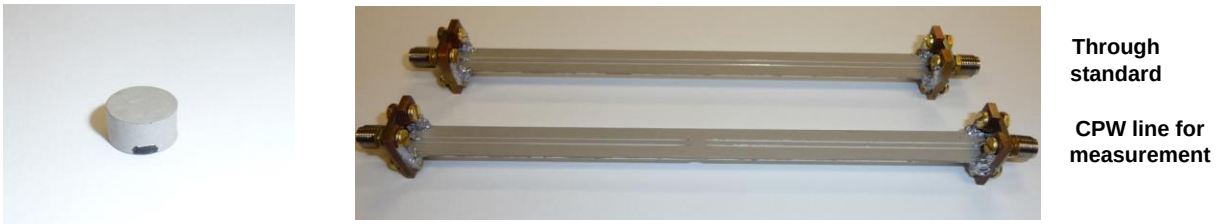

(b)

Fig. 1. (a) The Si_4B_1CN sample with Pt coating. (b) CPW lines for calibration and measurement.

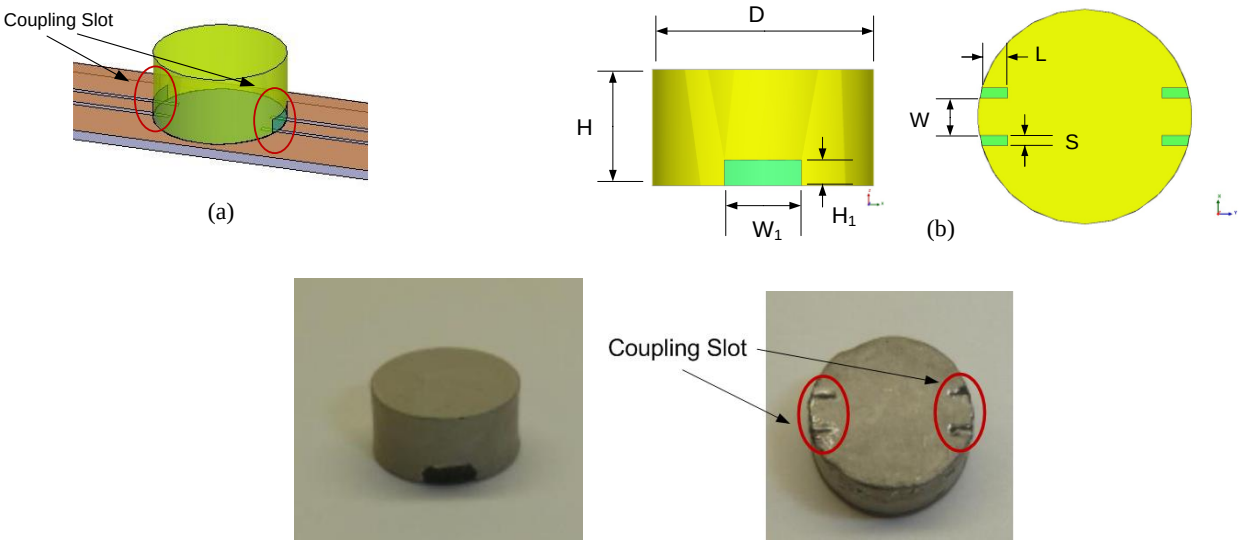

(a) (b)

(c)

Fig. 2. (a) Schematic of the resonator over CPW line. (b) Dimensions of the coupling slots. (c) Photos of sidewall and bottom with coupling slots. (D=9.37; H=4.71; W_1=3; H_1=1; W=1.5; L=1.35; S=0.4) (unit: mm)

Through calibration was conducted at room temperature before the measurements. The temperature of the resonator was increased from 25 to 1400°C during the measurement with a step of 50°C when the temperature was above 50°C. The measured S_{21} versus different temperatures are plotted in Fig. 3(a). f_r and Q_u versus temperature extracted from the measured S_{21} are plotted in Fig. 3(b) and (c), respectively. f_r decreases from 11.2 to 10.6 GHz and Q_u decreases from 85 to 19, when the temperature increases from 25 to 1300°C. At 1300°C the resonant peak is close to the noise floor and the Q_u reaches the lowest value of 19 in the measurement range. The resonant peak falls below the noise level above 1300°C. It is believed that this is not only due to the increased loss in the resonator but also largely due to the loss in the long CPW lines. The measured material properties of SiCN up to 1300°C is by far the best result and are very promising for the success of temperature/pressure sensor working up to 1300°C or above. The SiCN resonator and metallization appear to be intact after measurement up to 1400°C.

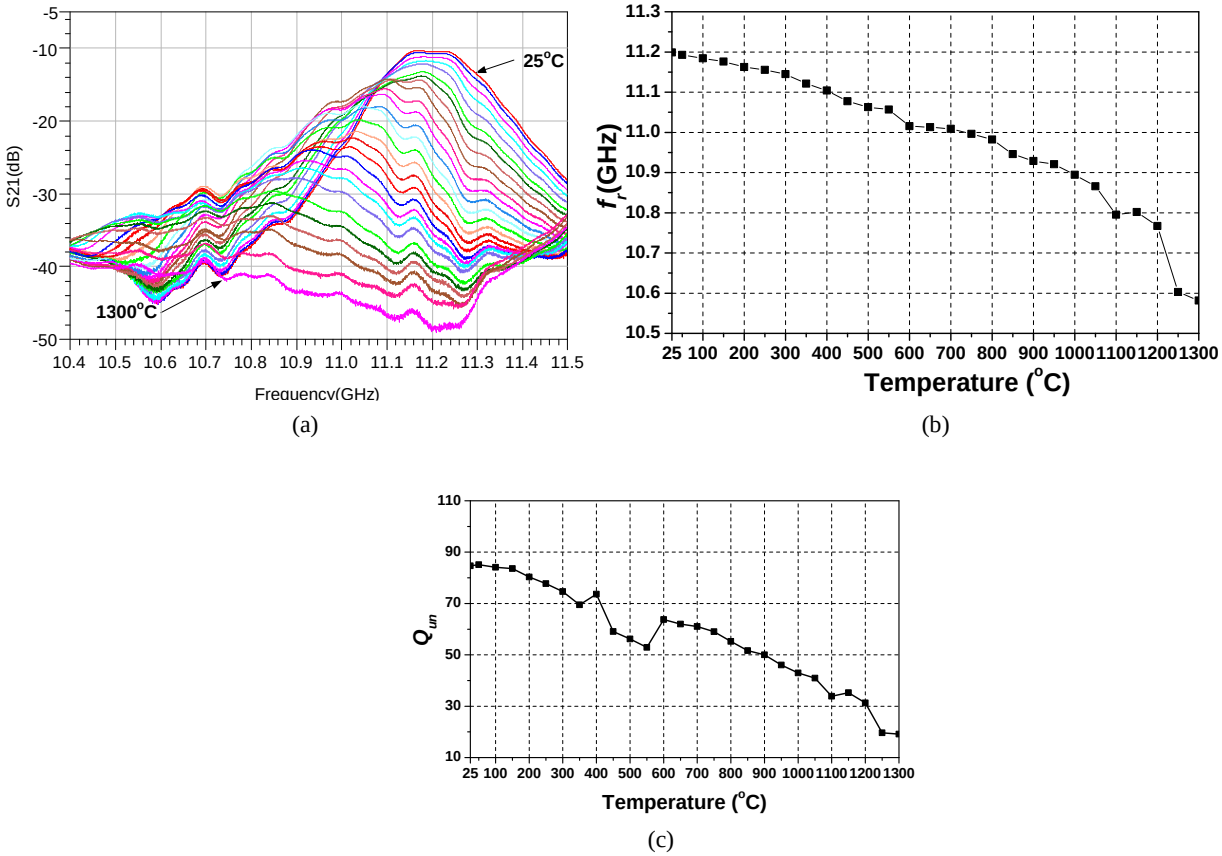

Fig. 3. (a) S_{21} from 25 to 1300°C. Extracted (b) f_r and (c) Q_u versus temperature.

2.2. Temperature Sensor

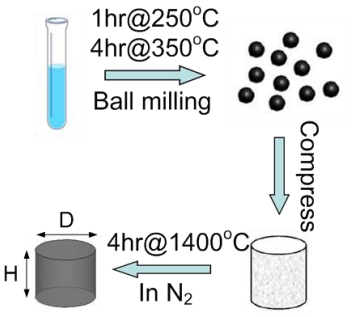

Fig. 4. Process flow of SiBCN ceramics in schematics.

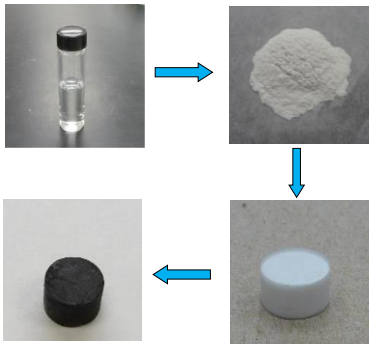

Fig. 5. Process flow of SiBCN ceramics in photos.

The SiBCN ceramics are synthesized by thermal decomposition of a commercially-available liquid-phase polysilazane (Ceraset, Kion, Huntingdon Valley, PA) as shown in Fig. 4 and Fig. 5. First, the precursor is solidified by heat treatment at 250°C for 1 hour, followed by heat treatment at 350°C for 4 hours in ultra-high-purity nitrogen. The obtained solids are then crushed and ball-milled into fine powders using high-energy ball milling. The powders are compressed into discs and then pyrolyzed at the temperature up to 1400°C for 4 hours in a tube furnace under a flow of ultra-high-purity nitrogen. In order to achieve better

dielectric property of SiBCN materials, boron-doped SiCN ceramics with different Si to B ratios are fabricated. Two sensors are fabricated and measured in this study. One is made of Si_6B_1CN (sintered at 1000ºC) and the other is made of Si_4B_1CN (sintered at 1100ºC). In order to form a waveguide cavity resonator, a layer of platinum paste (ESL 5542) is applied on all faces of the cylindrical samples. Then the samples covered by platinum paste are dried at 100 ℃ for 10 minutes and sintered at 1000 ℃ for 10 minutes. The ramp rate during the sintering is 10 ℃/min. The formed platinum layer is approximately 30 μm thick. The slot antenna is formed on the top surface of the cavity by milling process as shown in Fig. 6. The dimension of the fabricated sensors are shown in Fig. 7.

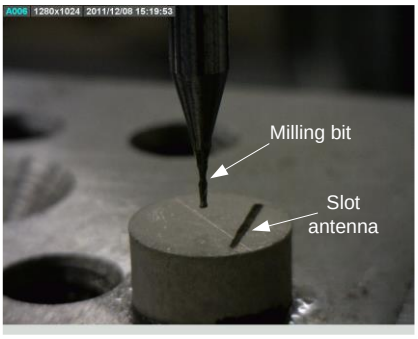

Fig. 6. Slot antenna fabrication by milling.

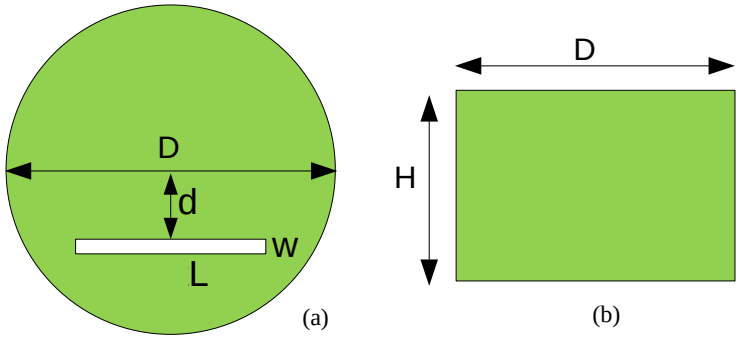

Fig. 7. (a)Top and (b) side views of the sensor and dimensions. (Si_6B_1CN (1000ºC): D=8.59, H=4.48, d=2.0, w=0.45, L=6.8; Si_4B_1CN (1100ºC): D=9.24, H=4.82, d=2.0, w=0.45, L=7.0) (unit: mm)

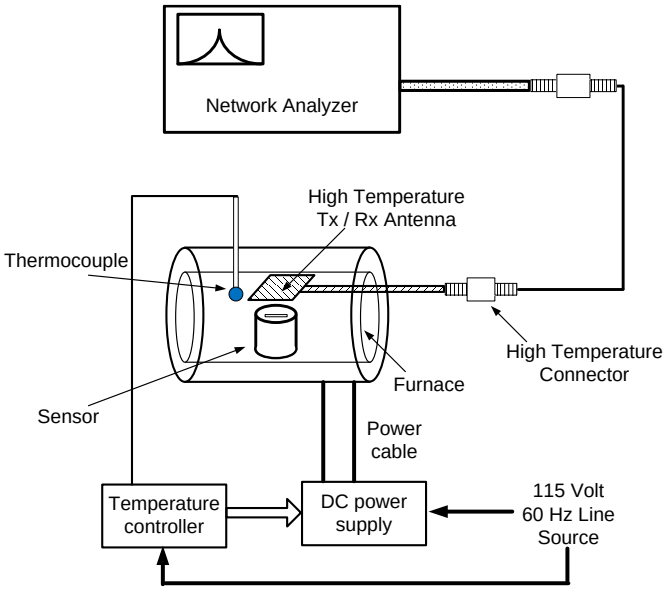

Fig. 8. Schematic of the measurement setup for the temperature sensor.

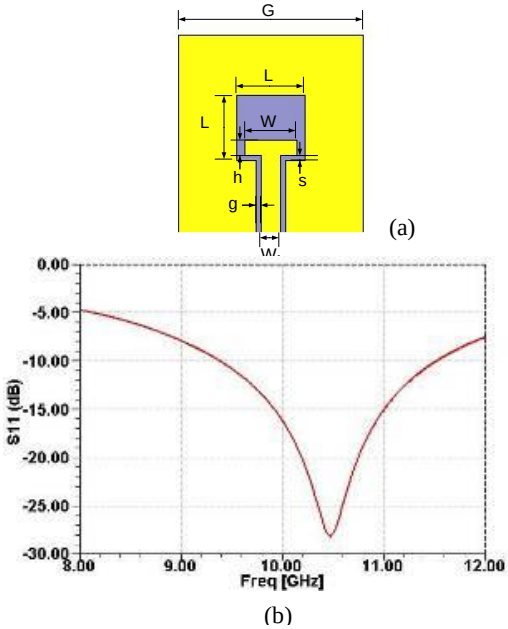

Fig. 9. (a) Dimension and (b) simulated S_{11} result of the antenna. G=23; L_1=8.4; L_2=8; W=6.4; h=1.9; s= 0.6; W_f=2.5. (Unit: mm)

The schematic of the measurement setup is shown in Fig. 8. The furnace is the same as the one we used for the material characterization. It can reach temperatures as high as 1500ºC with a resolution of ±2ºC. The sensor and antenna are in the furnace. The two ends of the furnace were sealed using alumina wool during the measurement. Therefore, the temperature inside the furnace is very stable. The antenna is connected to the network analyzer through a high temperature cable. The measured S_{11} can be read from

the network analyzer. However, the bulky *X*-band open-end waveguide cannot be directly put into the furnace. In addition, it cannot withstand the high temperature inside the furnace. Therefore, high temperature antenna is necessary for the sensor characterization. This high temperature antenna was fabricated on the alumina substrate (0.635 mm in thickness) with the Pt paste. The dimensions of the designed antenna are shown in Fig. 9(a). Fig. 9(b) shows the simulated S_{11} of the antenna. The center frequency of the antenna is 10.5 GHz with a fractional bandwidth of 20.2%, which can cover the entire operation frequency range of the temperature sensor.

The next step is to fabricate the high temperature antenna. First, the outline of the antenna is printed onto the alumina board and a layer of Pt paste (ESL 5542) is painted to form the antenna pattern. The antenna was sintered using the same aforementioned procedure. Fig. 10(a) shows the fabricated antenna. The measured S_{11} response of this antenna is plotted in Fig. 10(b). The bandwidth is from 9.57 to 10.66 GHz, which is sufficiently wide for sensor characterization.

(a)

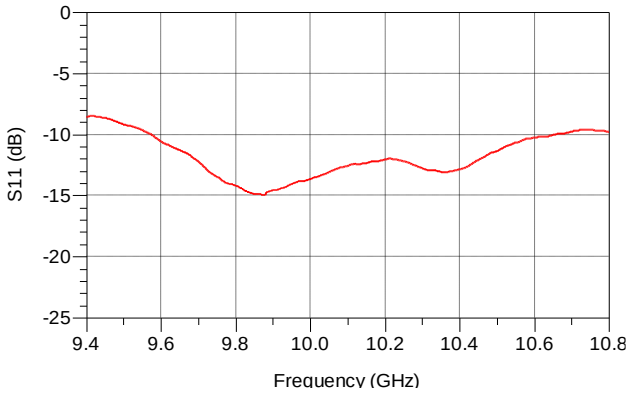

(b)

Fig. 10. (a) Fabricated high temperature antenna and (b) S_{11} response of the antenna.

Fig. 11 illustrates the measurement setup. The high temperature antenna is over the top of the sensor and used for the wireless sensing, as shown in Fig. 11(a). The distance between them is kept at 5 mm. One and half inches of the CPW line of the antenna stretches outside the furnace, so the connector at the end of the antenna feed line is at the low temperature. The inside of furnace is shown in Fig. 11(b). The sensor, antenna and K-type thermocouple are in the hot zone of the furnace, where the temperature can be up to 1500ºC.

The measurement is performed from 25 to 1300ºC. One port Short-Open-Load (SOL) calibration is done at the end of the coaxial cable, which is connected to the high temperature antenna. The proper time domain gating is applied onto the measured S parameters. The measured S_{11} results of high temperature antenna at different frequency for Si_4B_1CN (1100ºC) sensor are plotted in Fig. 12. Each curve represents a S_{11} response at one temperature in the 25-1300ºC range. There is a unique peak at the highest signal level. This peak corresponds to the resonant frequency of the sensor. As temperature increases, the resonant frequency and signal level decrease. Above the temperature of 1300ºC, the resonant peak is hard to be observed. According to the temperature dependent property of the materials, the resonant frequency of the sensor is expected to decrease monotonously with temperature. However, the resonant frequency at 1350ºC is higher than that at 1300ºC, as shown in Fig. 13. Because the loss of the Si_4B_1CN (1100ºC) material and platinum becomes larger with higher temperature, the re-radiated signal from the sensor becomes weaker. Therefore, the ripples appear on the S_{11} curve due to noise. It becomes harder to detect the resonant frequency at the temperature above 1300ºC. The resonant frequencies and Qs of this sensor are extracted and plotted in Fig. 14. The resonant frequency decreases from 10.52 to 9.92 GHz in the

temperature range of 25-1300ºC, which corresponds to a measured sensor sensitivity of 0.47 MHz/ºC. The highest Q is 34 at room temperature and the lowest Q is 10, which is observed at 1200ºC.

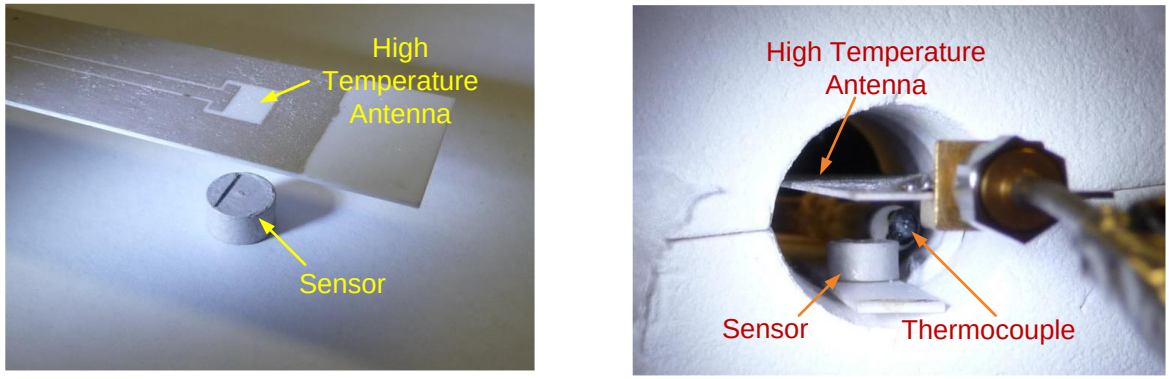

(a) (b)

Fig. 11. Si_4B_1CN (1100ºC) sensor and high temperature antenna (a) outside the furnace and (b) inside the furnace.

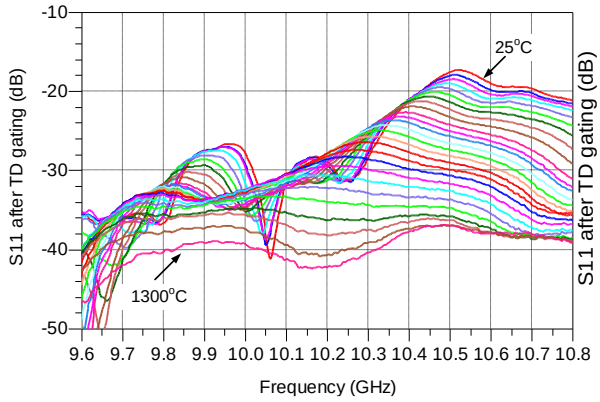

Fig. 12. Measured S_{11} responses of the Si_4B_1CN (1100ºC) sensor at different temperatures.

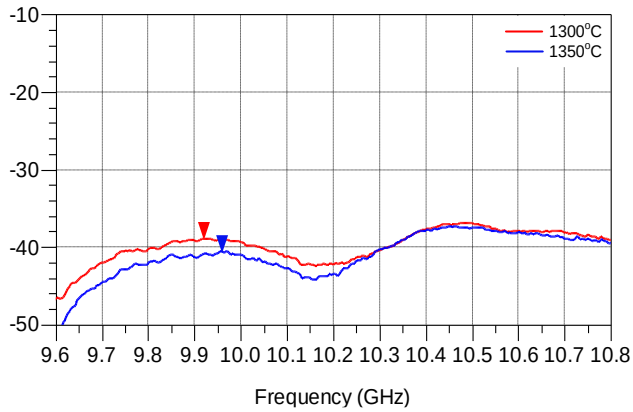

Fig. 13. Comparison between measured S_{11} responses of the Si_4B_1CN (1100ºC) sensor at 1300ºC and 1350ºC.

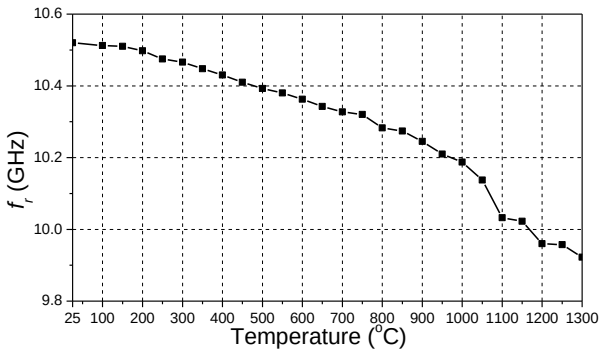

(a)

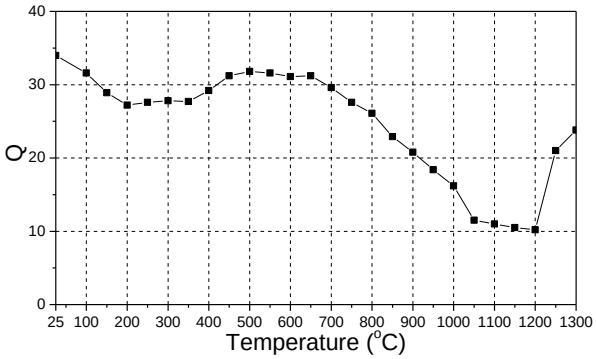

(b)

Fig. 14. Measured (a) resonant frequency and (b) Q of the Si_4B_1CN (1100ºC) sensor.

2.3. Pressure Sensor

Fig. 15 shows the polymer after the soft lithography. The polymer shape is formed by a Teflon mould fabricated by micromechanical machining. After sintering, the polymer turns into ceramic with black color. Platinum paste of approximately 25-μm thick is deposited on the ceramic bottom and shown in Fig. 16.

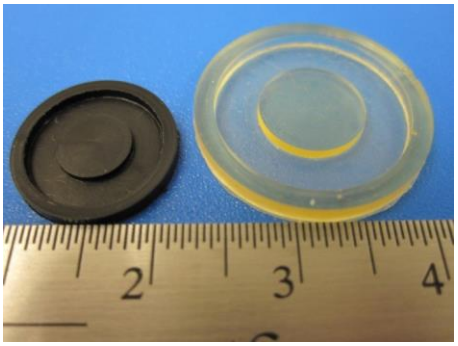

Fig. 15. Fabricated polymer (transparent) and sintered ceramic (black).

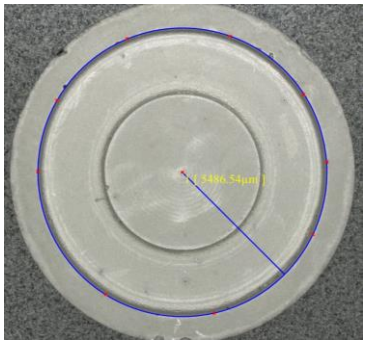

Fig. 16. After platinum metallization.

To design the dimension of the Teflon mould, experiments were carried out first to find out the shrinkage rate. By measuring the dimension of the mould and sintered ceramic, the shrink rate is found to be 68%. Therefore the dimensions for polymer are calculated and shown in Fig. 17. The micromachining tolerance is characterized using a digital microscope and shown in Table 1. Fig. 18 and 19 show the measurement results from the microscope, corresponding to the cavity edge and top of the post, respectively.

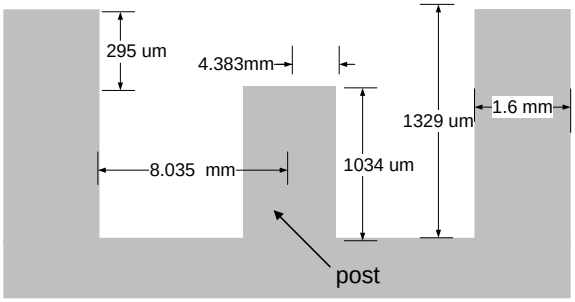

Fig. 17. Designed dimensions of the polymer by mould fabrication.

Table 1. The fabrication tolerance of the mould by micromechanical machining.

Designed	1034 μm	1329 μm	4.383 mm	8.035 mm	1.6 mm
Measured	1012 μm	1307 μm	4.39 mm	7.99 mm	1.607 mm

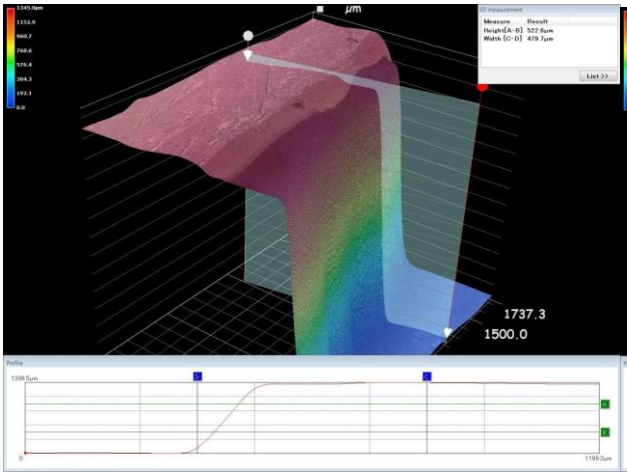

Fig. 18. Profile of the cavity edge of the mould.

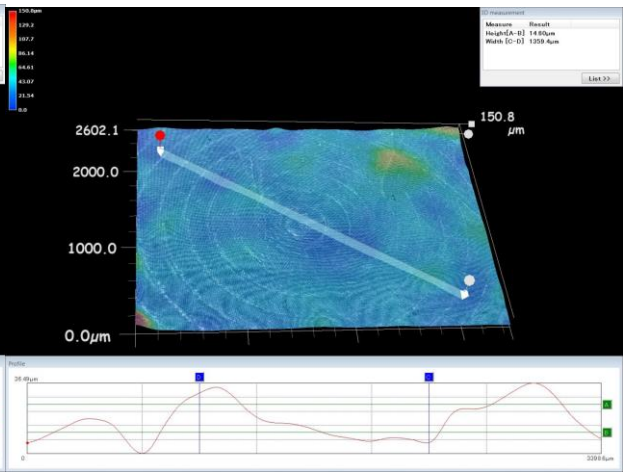

Fig. 19. Profile of the mould area corresponding to the post surface.

The cavity bottom after the metallization is measured by the Keyence digital microscope. The results are shown below in Figs. 20 and 21. The maximum deviation of the height on the post surface is 37 μm as shown in Fig. 22.

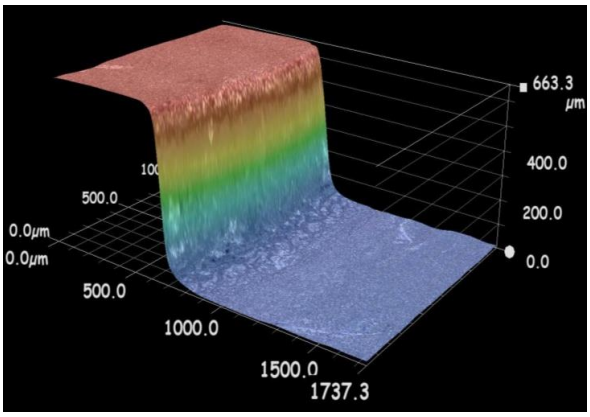

Fig. 20. Profile of the post of 0#.

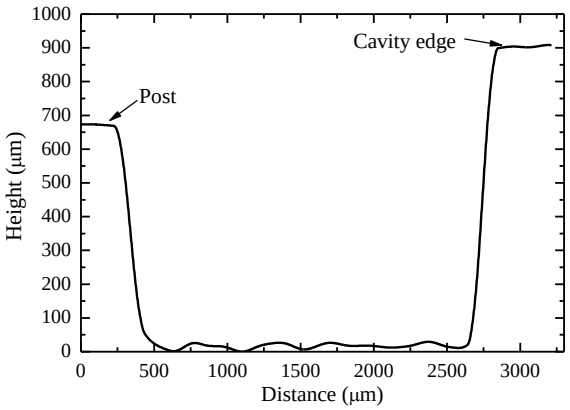

Fig. 21. Profile of the post and cavity edge for 0#.

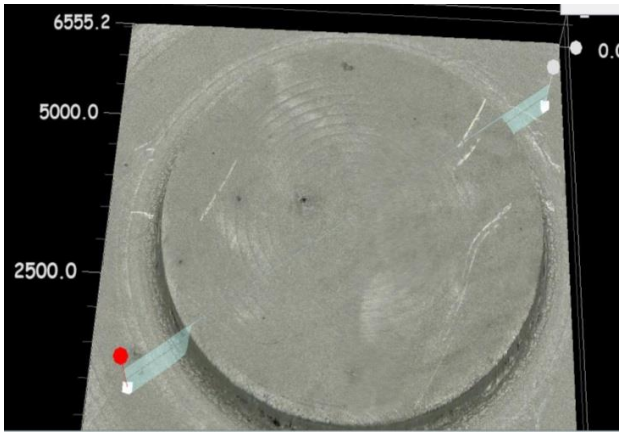

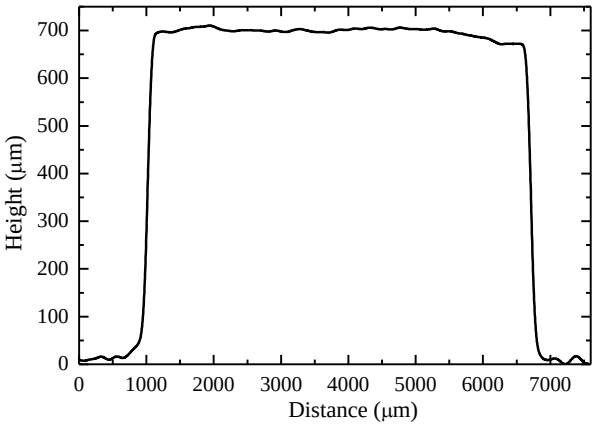

Fig. 22. Post photo (left) and profile (right) for 0#.

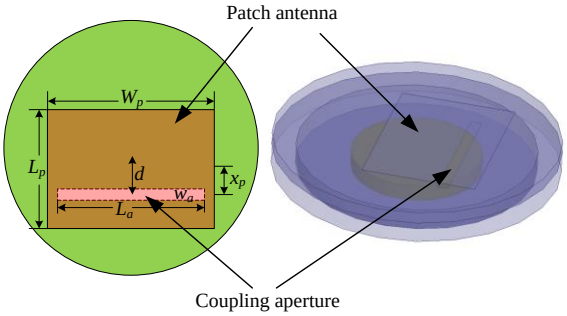

Fig. 23. Patch antenna for the pressure sensor. Top view (left) and 3-D view (right). The patch antenna is at the top surface of the pressure sensor cap. The coupling aperture drawn in dashed lines is at the bottom surface of the pressure sensor cap.

PDC with 10% PVN is used to build the pressure sensor cap due to its lower dielectric loss. The patch length L_p and width W_p are calculated first by using microstrip antenna theory at the resonant frequency of 11.9 GHz. For the ceramic substrate with thickness of 0.48 mm and ε_r = 5.36 (assuming 5% increase from ε_r = 5.1 at room temperature to 1000°C), L_p = 5.4 mm and W_p = 7.1 mm are obtained, respectively. The coupling aperture width and location are fixed as W_a = 0.5 mm and d = 2 mm during the antenna design. The coupling aperture length L_a and the patch antenna location X_p are studied, when an OEWG antenna is used to interrogate the sensor. The received signals versus the two parameters are shown in Figs. 24 and 25, respectively. L_a = 6 mm and X_p = 0.8 mm are chosen to achieve a good compromise between received signal strength and Q factor (higher Q factor leads to better frequency resolution). The dimensions of the patch antenna and coupling aperture are summarized in Table 2.

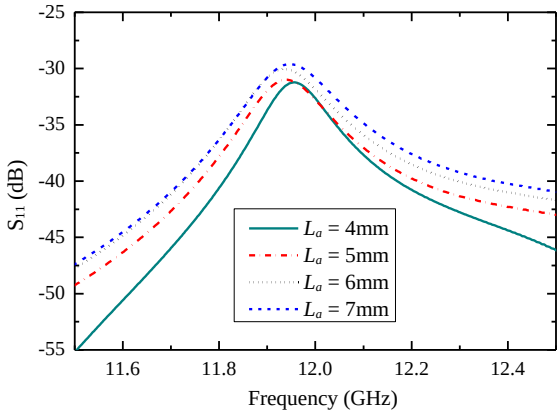

Fig. 24. Received signal strength versus L_a.

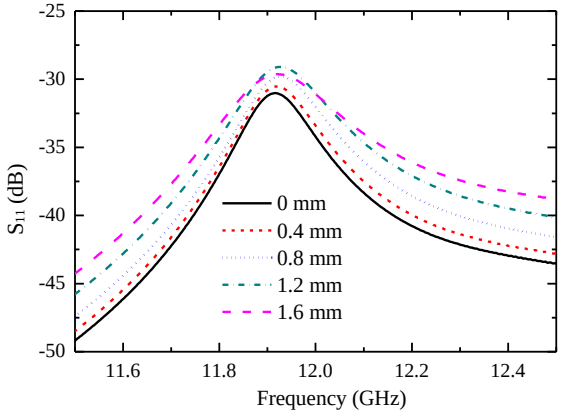

Fig. 25. Received signal strength versus X_p.

Table 2. Dimensions of the patch antenna and coupling aperture.

Antenna Parameters	Patch length L_p	Patch width W_p	Aperture width W_a	Aperture location d	Aperture length L_a	Patch offset X_p
Dimensions in mm	5.4	7.1	0.5	2	6	0.8

The interrogator antenna is redesigned at higher frequency, compared with previously-fabricated antenna working at 9.0-11.8 GHz. The antenna schematic is shown in Fig. 26. During the antenna design, the slot length L_s, slot width W_s, tuning-stub length L_t, and tuning-stub width W_t are studied, respectively. The spacing between the tuning stub and the slot edge is chosen as s = 0.6 mm. The air window is cut with the dimensions of 4×2.5 mm^2 by using laser machining. The antenna parameter study is shown in Figs. 27-30. The dimensions of the designed slot antenna are summarized in Table 3.

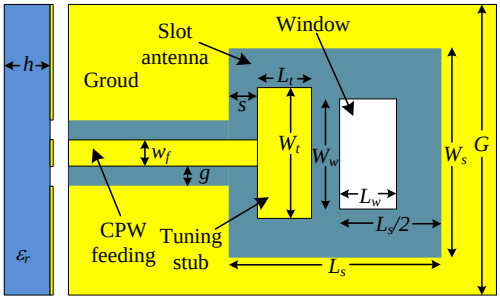

Fig. 26. Schematic of the interrogator antenna.

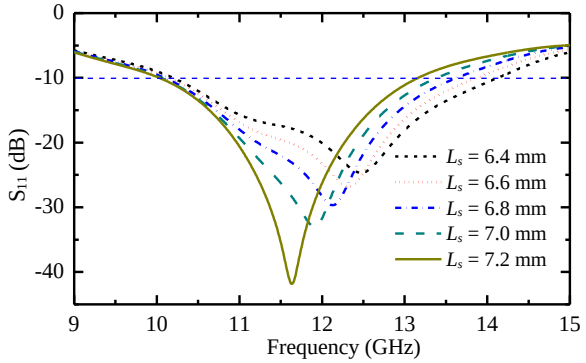

Fig. 27. Simulated S_{11} responses for the slot length L_s.

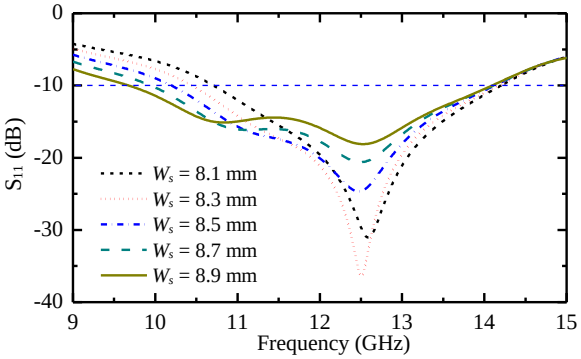

Fig. 28. Simulated S_{11} responses for the slot width W_s.

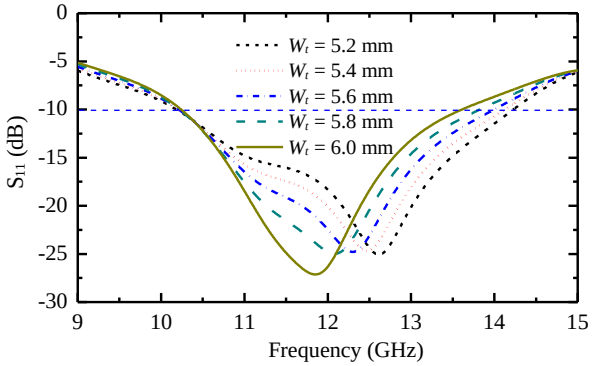

Fig. 29. Simulated S_{11} responses for the tuning-stub width W_t.

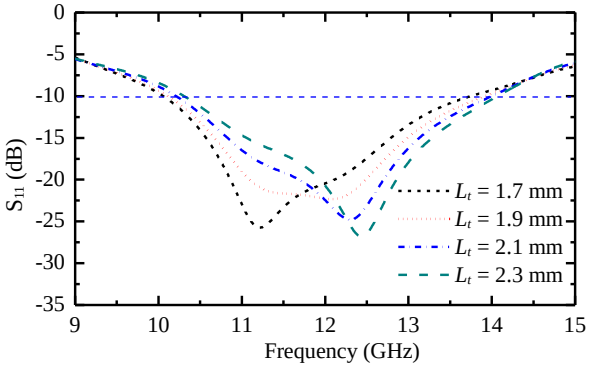

Fig. 30. Simulated S_{11} responses for the tuning-stub length L_t.

Table 3. Dimensions of the interrogator antenna.

Parameters	h	w_f	g	G	s	L_s	W_s	L_t	W_t	L_w	W_w
Dimensions (mm)	0.65	2.5	0.63	22.9	0.6	6.4	8.5	2.1	5.6	4	2.5

By using the same fabrication process for high-temperature antennas described earlier, this antenna is fabricated with platinum metallization on the alumina substrate. After TRL calibration, the measured S_{11} of the interrogator antenna is compared with the simulation as shown in Fig. 31. The measured fractional bandwidth is 31% at the center frequency of 11.8 GHz, which matches the simulation very well.

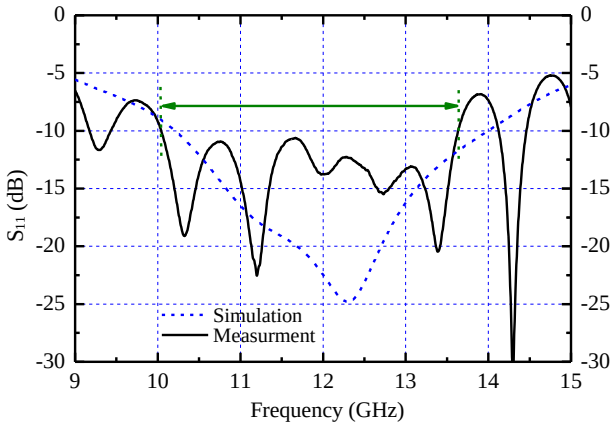

Fig. 31. Measured S_{11} of the interrogator antenna.

In this updated measurement setup, a stand is used to hold the force gauge in place to provide precise control of applied force on the pressure sensor. As shown in Fig. 32(a), the heat pad is used to control the temperature of the pressure sensor with the help from a thermal couple. The force on the pressure sensor is applied by an alumina rod, which is monitored by the force gauge. The resonant frequency change of the pressure sensor due to the deformation of the sensor cap can be characterized using a network analyzer. Fig. 32(b) illustrates the exploded view of the pressure sensor under test. The alumina rod passes through the open slot inside the interrogator antenna. With this updated measurement setup, the pressure and temperature can be independently and simultaneously applied to the sensor with precise control.

(a) (b)

Fig. 32. (a) Pressure sensor measurement setup. (b) Exploded view of the interrogator antenna and the sensor on the heat pad.

The pressure sensor is measured at different temperatures (up to 800°C) with various applied forces (up to 5N). The measured responses are shown in Fig. 33(a)-(d). The resonant frequency versus pressure is summarized in Fig. 33(e). It is observed that the resonant frequency decreases with the increasing applied force in a linear fashion. For example, the resonant frequency is reduced from 11.75 to 11.56 GHz when the external force increases from 0 to 5 Newton at 800°C. It should be noted that the resonant frequency is also affected by the temperature. Therefore, a temperature sensor is necessary to calibrate the frequency drift due to the temperature effect. The sensor signal becomes weaker at higher temperatures due to the higher dielectric and metallic losses at elevated temperatures.

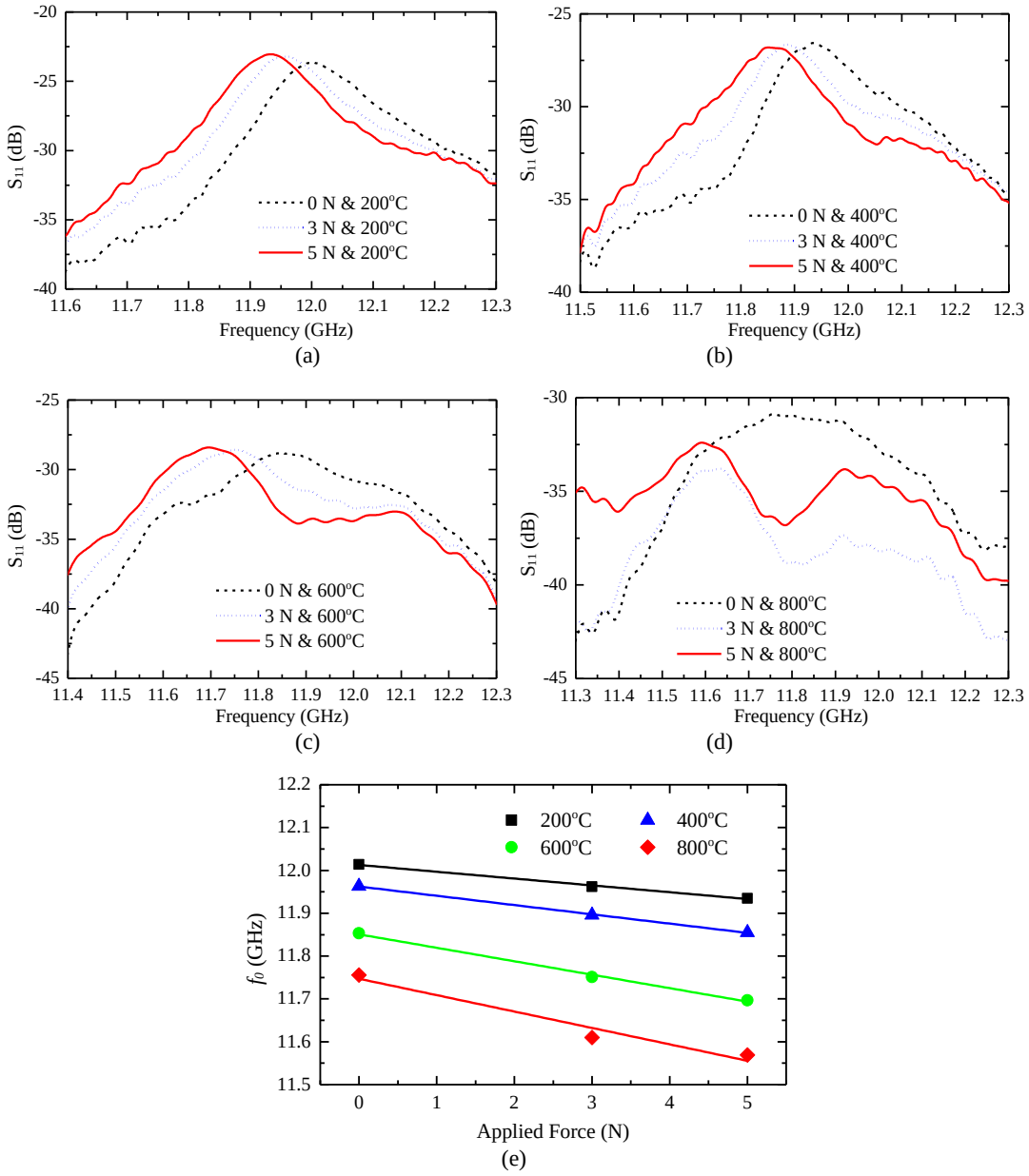

Fig. 33. The measured sensor responses with the applied force at different temperatures.

In order to understand the degree of deformation of the pressure sensor cap and estimate the change in the Young's modulus under different temperatures, both electromagnetic and mechanical analysis has been performed. Fig 34 shows the resonant frequency change of the pressure sensor versus the different gap dimensions caused by the cap deformation. For this pressure sensor based on the evanescent-mode cavity, the resonant frequency decreases with smaller gap dimensions. Also shown in the same figure, the sensor sensitivity is higher when the gap is smaller. By combining Figs. 33 and 34, the deformation versus applied force at different temperatures are extracted and plotted in Fig. 35. It is observed that at higher temperatures, more deformation occurs for the same amount of change in the applied force, which implies a change in the Young's modulus of the PDC. ANSYS simulation is used to analyze the mechanical behavior of the sensor as shown in Fig. 36. The sensor deformation for different Young's modulus is plotted in Fig. 37, corresponding to 3 and 5 N applied force, respectively. From Figs. 13 and 15, it is

found that the Young's modulus of the PDC ceramic (10% PVN) is reduced from 55 to 27 GPa from 200 to 800°C.

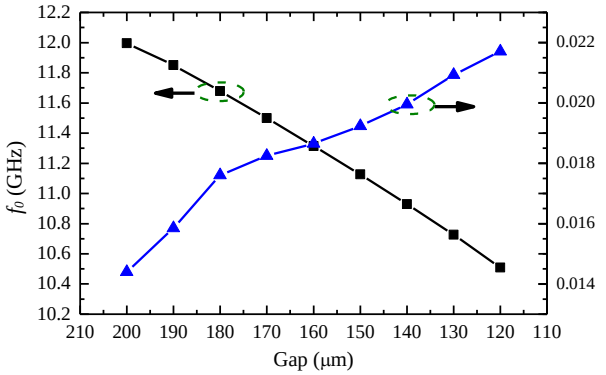

Fig. 34. Resonant frequency versus gap in HFSS simulation.

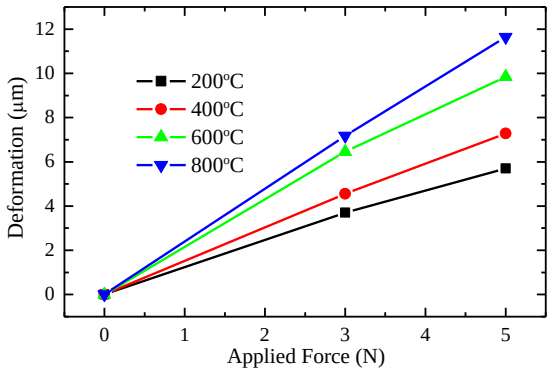

Fig. 35. Extracted cap deformation versus applied force.

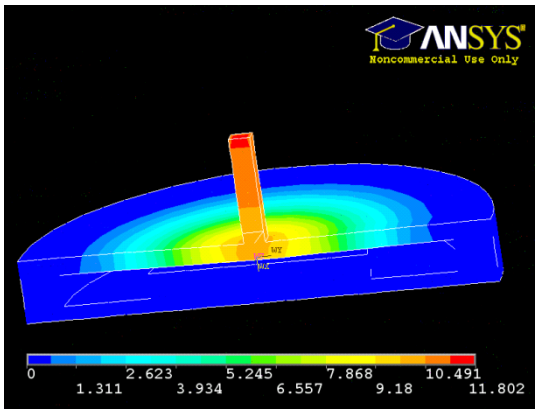

Fig. 36. Cap deformation simulation in the ANSYS.

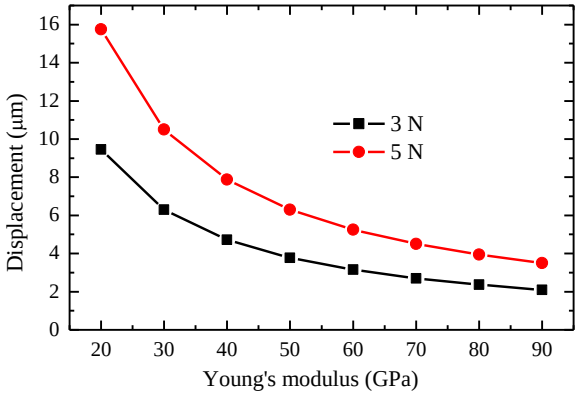

Fig. 37. Simulated cap deformation versus Young's modulus.

2.4. Wireless Sensing

At the beginning of this project, the wireless passive sensing was conducted using a high-speed digital oscilloscope (Tektronix DPO71604). However, the sensitivity and stability in measurement was not satisfactory. Therefore, alternative methods were sought after to realize good wireless passive sensing. One is the interrogator circuit built by one of my students, Jeff Lambert, by using Software-Defined Radio (SDR) technology. In this research effort, a functional *X*-band receiver using commercially-available components was developed and tested. It was shown that we have successfully detected the resonant frequency of a waveguide cavity resonator. The details for this interrogator development are in the master thesis written by Jeff Lambert, which is attached here for reference. However, improvements to the USRP are needed in order to enhance the measurement accuracy and speed. In parallel with Jeff Lambert's effort, other students supported by this DOE grant investigated the wireless passive sensing technology using network analyzer and time-domain gating technique. Very stable and accurate measurement results have been achieved for the aforementioned sensors by using this technique. All the results presented in this final report are from network analyzer measurement. It is worthy of noting that the network analyzer has limited output power and dynamic range, which limit the maximum wireless sensing range. The custom-designed interrogator, has the potential to achieve longer sensing range with higher power and lower noise floor if further development is performed.